Journal of Nondestructive Evaluation (2022) 41:35
https://doi.org/10.1007/s10921-022-00866-1

Evaluation of Ultrasonic SH-Waveform Tomography for Determining Cover Thickness and Rebar Size in Concrete Structures

Ruoyu Chen[1] · Khiem T. Tran[1] · Kien Dinh[2] · Christopher C. Ferraro[1]

Received: 15 April 2021 / Accepted: 18 March 2022

Abstract
The simultaneous detection of cover depth and rebar diameter are among the most frequently encountered issues for inspecting concrete for quality control and assurance, or evaluating a concrete structure. This paper presents a novel application of 2D full-waveform inversion of ultrasonic SH-waves (2D SH-FWI), for determining cover depth and size of embedded rebar. The method was applied to ultrasonic SH-wave datasets collected by a commercial shear-wave tomography system (MIRA) on four concrete specimens. Two of them had 10 steel bars of the same size (#5) embedded at various depths, and the other two had 10 steel bars of various sizes (#3 to #14) placed at the same cover depth of 65 mm. The results showed that the presented 2D SH-FWI was able to characterize both the depths and sizes of rebars. Except for the smallest rebar # 3, the difference between the inverted and true sizes is less than 30% for 9 rebars (#4 to #14 at 65-mm cover depth), and less than 33% for all 10 rebars (#5) at various depths from 25 to 140 mm. For comparison, the rebar sizes could not be obtained with the ultrasonic synthetic aperture focusing technique and GPR method, which only detected the cover thickness.

Keywords Concrete inspection · Cover thickness · Rebar diameter · Ultrasonic waveform tomography · SH-waves · NDT

1 Introduction

The identification of embedded steel rebar cover depth and size is one of the most commonly encountered problems in the inspection of reinforced concrete structures [1]. Usually, the information of interest includes the location of steel reinforcement, [2, 3], the concrete cover depth (or distance) [3–8], the bar size/diameter [7–13], and the likelihood/extent of rebar corrosion [14, 15]. The goal of this study was to develop a method that can effectively provide both the cover thickness and rebar diameter information using a commercially available ultrasonic pulse velocity (UPV) shear-wave tomography system (MIRA). The MIRA was selected for two reasons. First, this device is lightweight and can be handled easily on the construction site [16]. Second, but more importantly, the device utilizes a robust array of shear wave sensors to generate dense signal coverage and ray paths for each measurement. The relatively large amount of data, properly analyzed, provides information with respect to components and defects within reinforced concrete.

The use of Non-destructive testing (NDT) methods for the acquisition of rebar depth and rebar size has been researched quite extensively [3–13]. The majority of these research efforts were utilized NDT techniques such as pachometers and ground-penetrating radar (GPR) [5–13] and/or electromagnetic pulse induction [3, 8]. Pachometers are very useful for determination of depth of rebar and they can be used to determine the size of rebar. However, pachometers lack sensitivity at depth below 100 mm [17] and are not capable of determining size and location simultaneously. There has been little research performed where ultrasonic equipment utilized for determining rebar depth and size simultaneously [3, 4]. Although some of research has shown showed GPR can detect rebar size [7–13], the algorithms have not been fully validated for determination of all commonly used rebar sizes in concrete. Research involving the use of UPV has

✉ Khiem T. Tran
ttk@ufl.edu

Ruoyu Chen
chen.ruoyu@ufl.edu

Kien Dinh
kien@ndt-concrete.com

Christopher C. Ferraro
ferraro@ce.ufl.edu

[1] Department of Civil & Coastal Engineering, University of Florida, Gainesville, FL, USA

[2] NDT Concrete LLC, Deltona, FL, USA

Published online: 13 April 2022

focused on the determination of the concrete cover distance only. To our best knowledge, there have been no reported studies using the ultrasonic techniques for determination of rebar diameter.

With respect to data processing algorithm, full-waveform inversion (FWI) is a very promising approach for imaging reinforcement embedded in concrete. This method has been developed in the geophysics community and applied to image subsurface structures [18]. Using the complete content (waveform) of measured data, FWI produces high-resolution images of test objects than approaches that consider only portions of the measured wavefield such as the first-arrival signals or dispersion properties. Substantial progress on 2D and 3D FWI methodologies for seismic waves (< 50 Hz) has been made, at various scales from meters to kilometers (e.g., 2D FWI: [19–27], and 3D FWI: [28–41]).

The FWI approach has also been used on ultrasonic wavefields for nondestructive testing at smaller scales of millimeters to decimeters [42–44]. A few studies have been performed using 2D FWI for imaging of structural concrete, using synthetic and field experimental data with ultra-seismic wavefields at 500–2000 Hz [45, 46] and ultrasonic wavefields at 20–100 kHz [47] for evaluation of bridge abutments and decks, respectively. These studies utilize the elastic wave equations of vertical P- and S-waves (P-SV waves).

In this study, we present a novel application of a recently developed 2D SH-FWI method [48] on ultrasonic wavefields for concrete structural imaging, particularly for determination of rebar location and size. Both mass density and S-wave velocity are extracted to increase credibility of the characterized images. Compared to P-SV waves, simulation of SH-wave requires fewer input parameters, and the required computer time for the SH-FWI is approximately 50% of that of P-SV waves. The method was tested on four reinforced concrete slabs with embedded rebar of various sizes and depths, and results are compared to those of the conventional synthetic aperture focusing technique (SAFT) [49] and GPR methods to assess the improvements.

2 Research Methodology

The 2D SH-FWI method [48] has recently been developed for geotechnical site characterization at meter-resolution. It relies on the solution of 2D elastic SH-wave equations in the time domain for the forward modelling to generate synthetic waveforms, and the adjoint-state gradient method with Tikhonov regularization technique to match observed (measured) and synthetic waveforms for model updating to extract material property images. The method is briefly documented for ultrasonic wavefields. For the forward modelling, the ultrasonic wavefields are simulated using the SH-wave equations [50] as:

$$\rho(x,\, z)\frac{\partial v_y}{\partial t} = \frac{\partial \sigma_{xy}}{\partial x} + \frac{\partial \sigma_{yz}}{\partial z} + f_y \tag{1}$$

$$\frac{\partial \sigma_{xy}}{\partial t} = \mu(x,\, z)\frac{\partial v_y}{\partial x} \tag{2}$$

$$\frac{\partial \sigma_{yz}}{\partial t} = \mu(x,\, z)\frac{\partial v_y}{\partial z} \tag{3}$$

where v_y is the particle velocity, σ_{xy} and σ_{yz} are shear stress, $\rho(x,\, z)$ is the mass density, f_y is the body force in y-direction, and $\mu(x,\, z)$ is the shear modulus. The 2D time-domain finite-difference scheme [50] is adopted to solve Eqs. (1) to (3). The free surface condition is applied at the top boundary with stress-imaging technique [51], and the perfectly matched layers [52] are implemented at the bottom and vertical boundaries to diminish the noise created by outgoing waves. See [48] for detailed description of the forward modelling. The model updating includes the following steps:

1. Calculate residual between estimated and observed waveform data:

$$\Delta \boldsymbol{d}_{t,r} = \boldsymbol{D}_{t,r}(\mathbf{m}) - \boldsymbol{d}_{t,r}, \tag{4}$$

where $\mathbf{m}$ is the model parameters, which are V_S and density. $\boldsymbol{D}_{t,r}(\mathbf{m})$ is the estimated ultrasonic data corresponding to model $\mathbf{m}$ from the forward modelling, and $\boldsymbol{d}_{t,r}$ is the observed (measured) ultrasonic data from lab or field experiment. Subscripts t, r denote the t-th transmitter (source) and r-th receiver.

2. Compute the least-squares error E($\mathbf{m}$):

$$\mathrm{E}(\mathbf{m}) = \frac{1}{2}\Delta \boldsymbol{d}^T \Delta \boldsymbol{d}, \tag{5}$$

where $\Delta \boldsymbol{d}$ is a column vector combining residuals $\Delta \boldsymbol{d}_{t,r}$ from all transmitters and receivers. T denotes the vector transpose.

3. Compute the gradients for S-wave velocity (V_S) and density (ρ) based on the adjoint-state method [53] as:

$$\frac{\partial E}{\partial V_s} = -\frac{2}{V_s^3 \rho}\sum_{i=1}^{N}\int_0^T dt(\sigma_{xy}^f \sigma_{xy}^b + \sigma_{yz}^f \sigma_{yz}^b), \tag{6}$$

$$\frac{\partial E}{\partial \rho} = -\frac{1}{V_s^2 \rho^2}\sum_{i=1}^{N}\int_0^T dt(\sigma_{xy}^f \sigma_{xy}^b + \sigma_{yz}^f \sigma_{yz}^b + V_s^2 \rho^2 \frac{\partial v_y}{\partial t} u_y^b), \tag{7}$$

where N denotes the number of transmitters. Parameters σ_{xy}^f and σ_{yz}^f represent the shear stresses in the forward-propagated wavefield, σ_{xy}^b and σ_{yz}^b represent the shear stresses in the back-propagated wavefield by propagating residuals from receivers. Parameter v_y indicates the

particle velocity in the forward wavefield and u_y^b indicates the particle displacement in the back-propagated wavefield.

4. Apply Tikhonov regularization [54] to mitigate the ill-posed inverse problem through smoothing the gradients as:

$$\left(\frac{\partial E}{\partial V_s}\right)_r = \frac{\partial E}{\partial V_s} + \lambda_1 \boldsymbol{L} V_s \tag{8}$$

$$\left(\frac{\partial E}{\partial \rho}\right)_r = \frac{\partial E}{\partial \rho} + \lambda_2 \boldsymbol{L} \rho \tag{9}$$

where **L** is the 2D Laplacian matrix. Coefficients λ_1 and λ_2 are the scaling factors between the regularization term and the gradient term.

5. Update S-wave velocity and density iteratively along the steepest-descent directions [55] as:

$$V_{s_{n+1}} = V_{s_n} - \alpha_n \boldsymbol{H}_n^{-1} \left(\frac{\partial E}{\partial V_s}\right)_r, \tag{10}$$

$$\rho_{n+1} = \rho_n - \beta_n \boldsymbol{H}_n^{-1} \left(\frac{\partial E}{\partial \rho}\right)_r, \tag{11}$$

where n denotes the iteration number, α_n and β_n are the optimal step lengths for V_S and ρ, respectively and obtained independently by parabolic fitting [55]. $\boldsymbol{H}_n^{-1}$ represents the inverse of Hessian matrix, it is calculated as the second derivative of the objective function. It is costly to implement the true Hessian, and thus its approximation [56] is adopted as:

$$\boldsymbol{H}_n^{-1} = \left\{\lambda + \sqrt{W_t(x, x_t) W_r(x)}\right\}^{-1}, \tag{12}$$

where

$$\lambda = 0.1 max_x \left\{\sqrt{W_t(x, x_t) W_r(x)}\right\}, \tag{13}$$

where x_t denotes the location of transmitter. $W_t(x, x_t)$ and $W_r(x)$ are the wave energy of the forward-propagated wavefield and the back-propagated residual wavefield at location x, respectively. Factor λ is used to avoid the inverse of infinitesimals.

6. Repeat steps 1–5 until the inversion meet the termination criteria, which for this work is defined as the maximum number (40) of iterations is reached or the change of the least-squares error E(**m**) less than 1% between previous and current iterations. See [48] for detailed description of the model updating.

3 Experiments

The experimentation was conducted at the structural engineering laboratory in the main campus of the University of Florida in Gainesville, Florida (USA). For the validation testing of this research, four concrete slab specimens were fabricated using two separate formwork designs (Fig. 1). Slabs have the same dimensions of 1150 × 550 × 190 mm, as shown in Fig. 2. One of the formworks had rebars with different diameters from #3 to #14 (English sizes) (Fig. 1a). The second formwork had rebar with various embedded depths from 25 to 140 mm (Fig. 1b). The concrete was cast in two separate placements using each formwork (two concrete slab specimens per placement), and the formwork was removed 3 days after casting.

The NDT data was collected using a commercial ultrasonic shear-wave tomography system, which is known as the MIRA tomographer as shown in Fig. 3. The device has 48 ultrasonic transducers located in a 12 × 4 grid at 3 cm spacing (12 rows of 4 transducers each). The transducers work as both transmitters and receivers in a sequential mode.

Data acquisition using the MIRA device included measurements along the central line (length) for each slab. The ultrasonic data was collected at a total of five locations every 200 mm. For each test location, the first wavefield induced by the first row of transducers (4 transducers acting as transmitters simultaneously) was recorded by the eleven remaining rows of transducers (rows 2 to 12). The second wavefield was induced by the second row of transducers is only recorded by the ten remaining rows of transducers (row 3 to 12). Based on the reciprocity, the wavefield is identical if the transmitter and receiver are switched locations. The second wavefield recorded by the first row is the same as the first wavefield recorded by the second row, thus there is no need for redundant measurements. The process was continued until the last wavefield induced by the 11-th row of transducers and recorded by the 12-th row of transducers. For each test location, a total of 66 measurements were recorded for the total recording time of 0.6 ms with a sampling rate of 1 microsecond.

3.1 Analysis of a Sample Dataset

The analysis of one sample dataset is presented in detail to demonstrate the capability of the presented SH-FWI algorithm. The data was collected at a location on a slab as shown in Fig. 3a and b for the top and side views, respectively. The MIRA scanning area includes three rebars with sizes of #6, #5 and #4 from left to right, respectively. The data was filtered through the frequency bandwidth of 20 to 70 kHz, and signals outside of the selected bandwidth were not consistent, and thus removed from the analysis. Shown in Fig. 4a is the measured waveform data in the time domain induced by the first

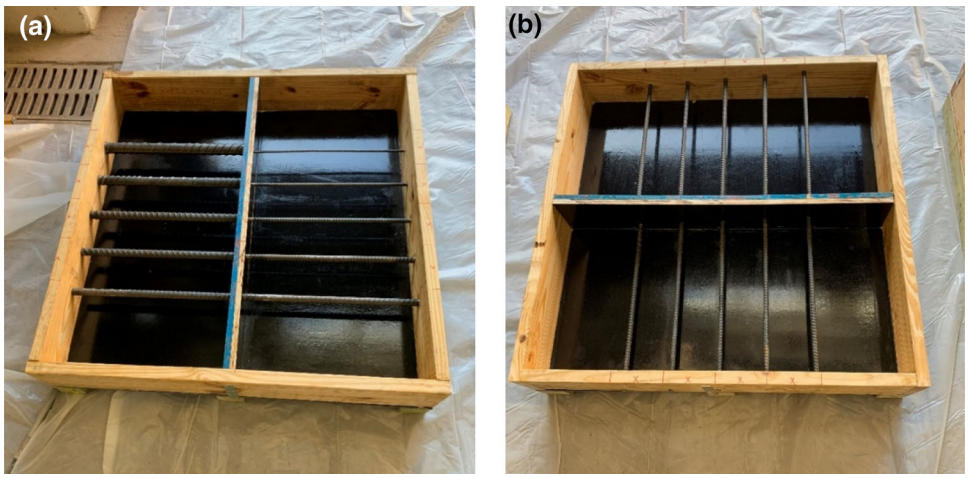

Fig. 1 The formworks used for concrete slab casting: **a** rebars with different sizes, and **b** rebars with different embedded depths

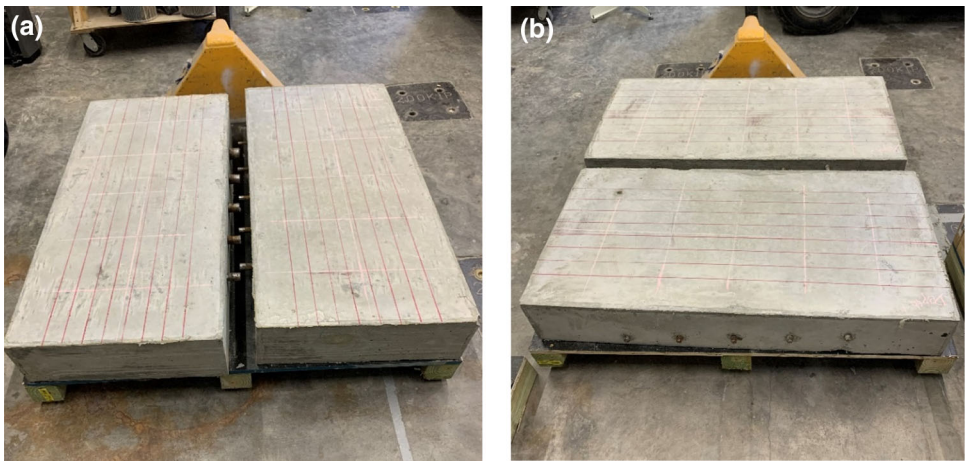

Fig. 2 The finished concrete slabs: **a** rebars with different sizes, and **b** rebars with different depths

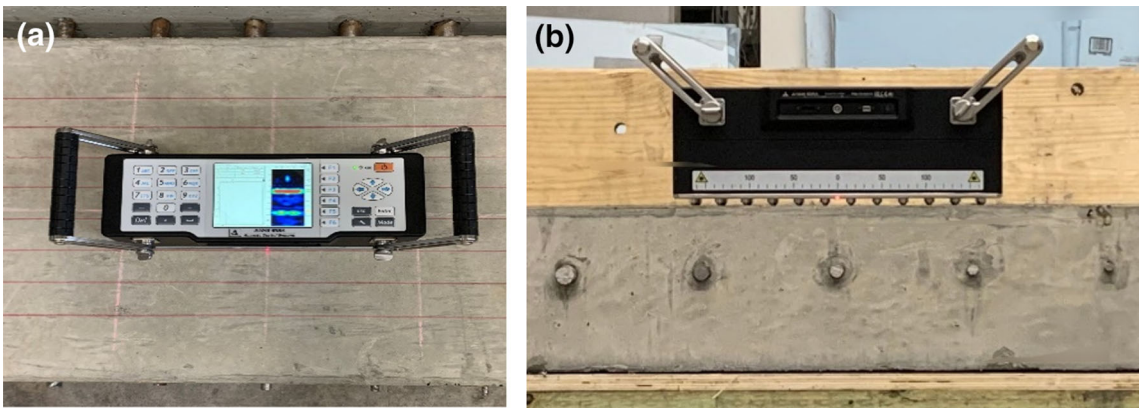

Fig. 3 The MIRA used for data sampling: **a** top view, and **b** side view

row of transmitters, and its corresponding frequency spectrum with the central frequency of approximately 45 kHz.

The medium of 350 mm × 200 mm (length × depth) was used for the SH-FWI analysis. The length was selected based on the MIRA transducer grid length of 330 mm (11 spaces of 30 mm) and 10 mm added in each side. The medium depth of 200 mm was intentionally chosen thicker than the true thickness (190 mm) of concrete slabs to conveniently handle the bottom boundary. The perfectly matched layer (PML) was implemented at the bottom and two vertical boundaries of the medium to absorb outgoing waves of simulated wavefields. The advantages of this approach include that: (1) the true thickness of slab is not required for analysis, (2) the

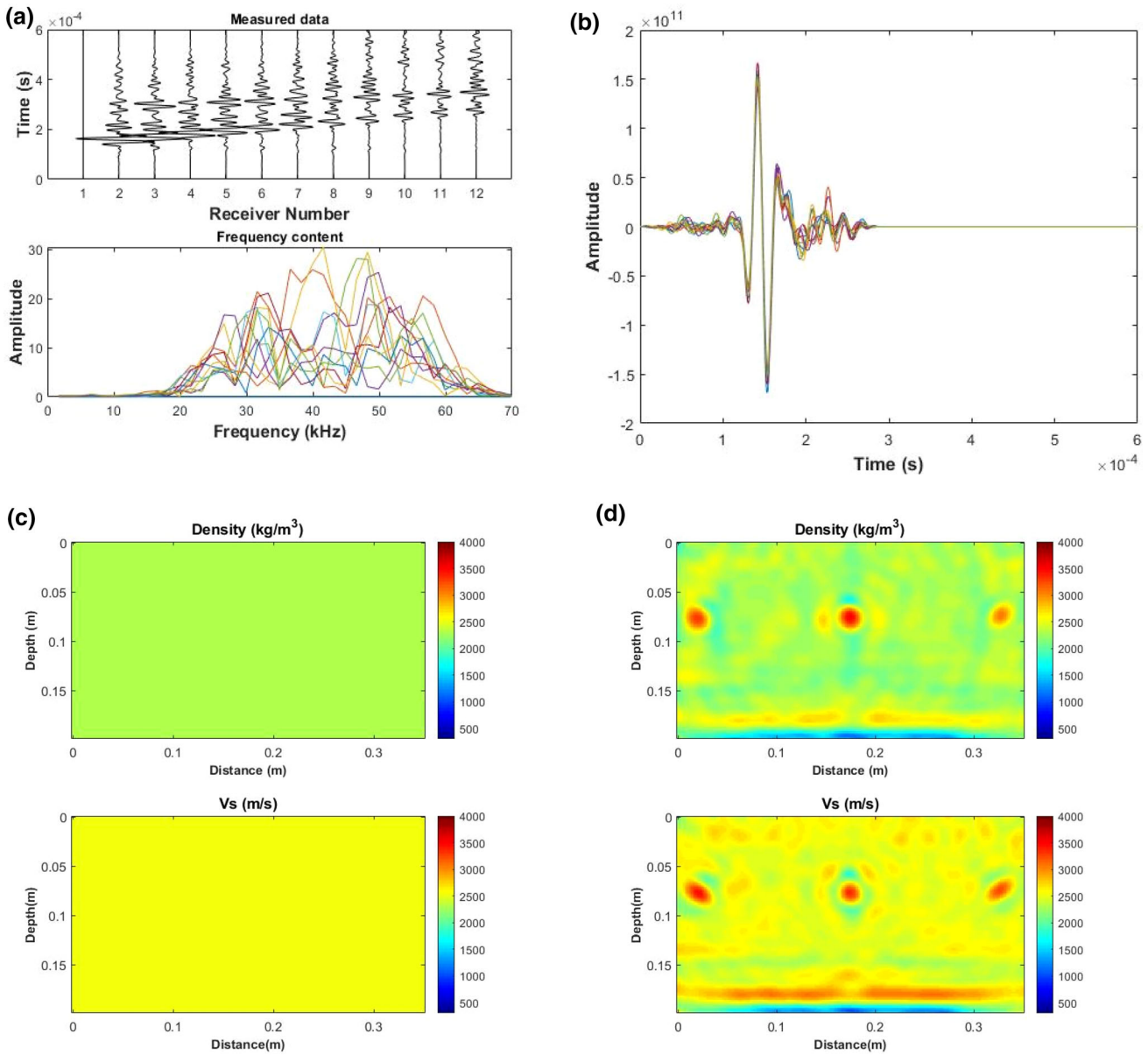

Fig. 4 Experiment: **a** the measured waveform and frequency distribution, **b** the estimated source signatures associated with the initial model, **c** the homogenous initial model based on measured Vs and density of concrete, and **d** final inverted result

free surface condition at the bottom boundary is not required to implement in the forward simulation, and (3) the slab thickness can be interpreted from the inverted result. The medium was discretized into 2 × 2-mm cells for both the forward modelling and model updating. The cell size of 2 mm was selected to maintain at least 10 grid points per minimum wavelength for accurate wave simulation, and provide desired high-resolution inverted images.

For inversion, appropriate initial models for both V_S and density are needed to avoid local solutions caused by the cycle skipping (matching of wrong waveform peaks). For V_S, the initial model was determined from V_S values provided by the MIRA system, which were approximately from 2490 to 2530 m/s at different sampling locations. The initial model of V_S was selected as a homogenous model of 2500 m/s (Fig. 4c, bottom). The initial model of density was determined through the direct measurement of concrete specimens. Three cylindrical concrete specimens were made during slab casting, and the average density measured from these specimens was approximately 2300 kg/m^3 that was used as the initial model of density (Fig. 4c, top). It is noted that density of 2300 kg/m^3 is the typical value for concrete density, and can be assumed for waveform analysis, in case of no direct measurement of density.

The source signature (pulse induced by a transmitter) was estimated based on the method proposed for GPR data [57] and for seismic data [47]. A Ricker wavelet that has the central frequency of the filtered measured data is used as an assumed source for the forward simulation to derive the Green's function $\boldsymbol{G}(f, x, \boldsymbol{m})$ associated with the model $\boldsymbol{m}$ as:

$$\boldsymbol{G}(f, x, \boldsymbol{m}) = \frac{\boldsymbol{D}(f, x, \mathbf{m})}{\boldsymbol{W}(f)}, \tag{14}$$

where x indicates the location for a transmitter and receiver pair, $\boldsymbol{D}(f, x, \boldsymbol{m})$ and $\boldsymbol{W}(f)$ represent the synthetic wavefield and source signature at frequency f, respectively. It is noted that any smooth wavelets can be used for the forward simulation to compute the Green's function. The estimated source was then calculated as $\boldsymbol{West}(f) = \boldsymbol{d}(f, x, \boldsymbol{m})/\boldsymbol{G}(f, x, \boldsymbol{m})$ in the frequency domain, where $\boldsymbol{d}(f, x, \boldsymbol{m})$ is the measured wavefield. As there are many pairs of transmitters and receivers, the least-squares technique of solving the overdetermined system of equations [58] was applied to determine the best source among all transmitter–receiver offsets. Finally, the frequency-domain source was transformed to the time domain, and used for the forward simulation. Figure 4b represents the estimated source signatures for all transmitters associated with the initial model. Both magnitude and phase of the source were determined, and their similarity suggests the consistent wave energy generated by the MIRA.

To account for the attenuation in the measured waveforms, a calibration function [59] was applied for correcting the estimated waveform data:

$$y(r) = Ar^b \tag{15}$$

where r corresponds to the transmitter–receiver offset, the factor A and exponent b were determined by minimizing the energy of waveform residuals. This calibration function was determined at the beginning of each run, and kept constant during inversion.

Density and V_S models were updated simultaneously and independently during inversion. The inversion stopped when it reached the predefined maximum iterations of 40. The running time for the entire inversion is approximately 20 min on a desktop computer (Dell Precision, 40 cores of 2.0 GHz each, 1.0 TB RAM). The least-squares error for the entire inversion is shown in Fig. 5. It decreases gradually from 1204 at the beginning to 202 at the end of analysis.

The comparison between the measured data and estimated data associated with the initial model, and the initial residuals are provided in Fig. 6a and c, respectively. No information with respect to the reinforcement and concrete-air interface

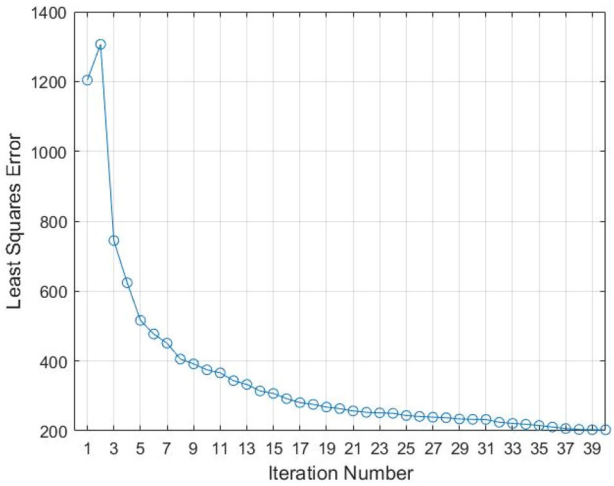

Fig. 5 Least-squares error versus the iteration number

(back-wall) is included in the initial model, no signal reflections were produced. Conversely, signal reflections exist in the measured data, but not in the initial estimated data, they remain in the initial residuals (Fig. 6c). The residuals clearly show the reflections from the reinforcement and back-wall. Shown in Fig. 6b and d are the comparison between the measured data and the final estimated data associated with the final inverted model, and the final residuals, respectively. The waveform match improved considerably during inversion from Fig. 6a, b, and the measured and final estimated data provided a reasonable fit for each of the channels. As the reinforcement and back-wall were inverted, the signal reflections from them existed in the estimated data, and thus the residuals decreased significantly for all channels, from Fig. 6c, d.

The final inverted result is shown in Fig. 4d, where three embedded rebars are imaged accurately in both density and V_S models. The inverted reinforcement has V_S of ~ 3000–3500 m/s, accompanying with the density ~ 3500–4000 kg/m^3. The inverted V_S value is around the true V_S value of steel, however, the inverted density is lower than its true value of about 7800 kg/m^3. This is due to two reasons: (1) the used initial value of 2300 kg/m^3 is too far off the true density of steel, and (2) the adopted Tikhonov regularization smooths the gradient that leads to constrained parameter updating. In addition, the inverted reinforcement at left and right sides are not circular due to the limited signal coverage since those reinforcing steel rebars are near the edges of the MIRA device as shown in Fig. 3b. The concrete-air interface is located at 0.19 m, which is consistent with the true slab thickness as the air layer starts from the depth of 0.19 m to the model bottom. Instead of zeros values, the inverted V_S and density values of air layer are close to 500 m/s and 500 kg/m^3, respectively. This is because of no signals passing through the zone below the slab, and the analysis can only

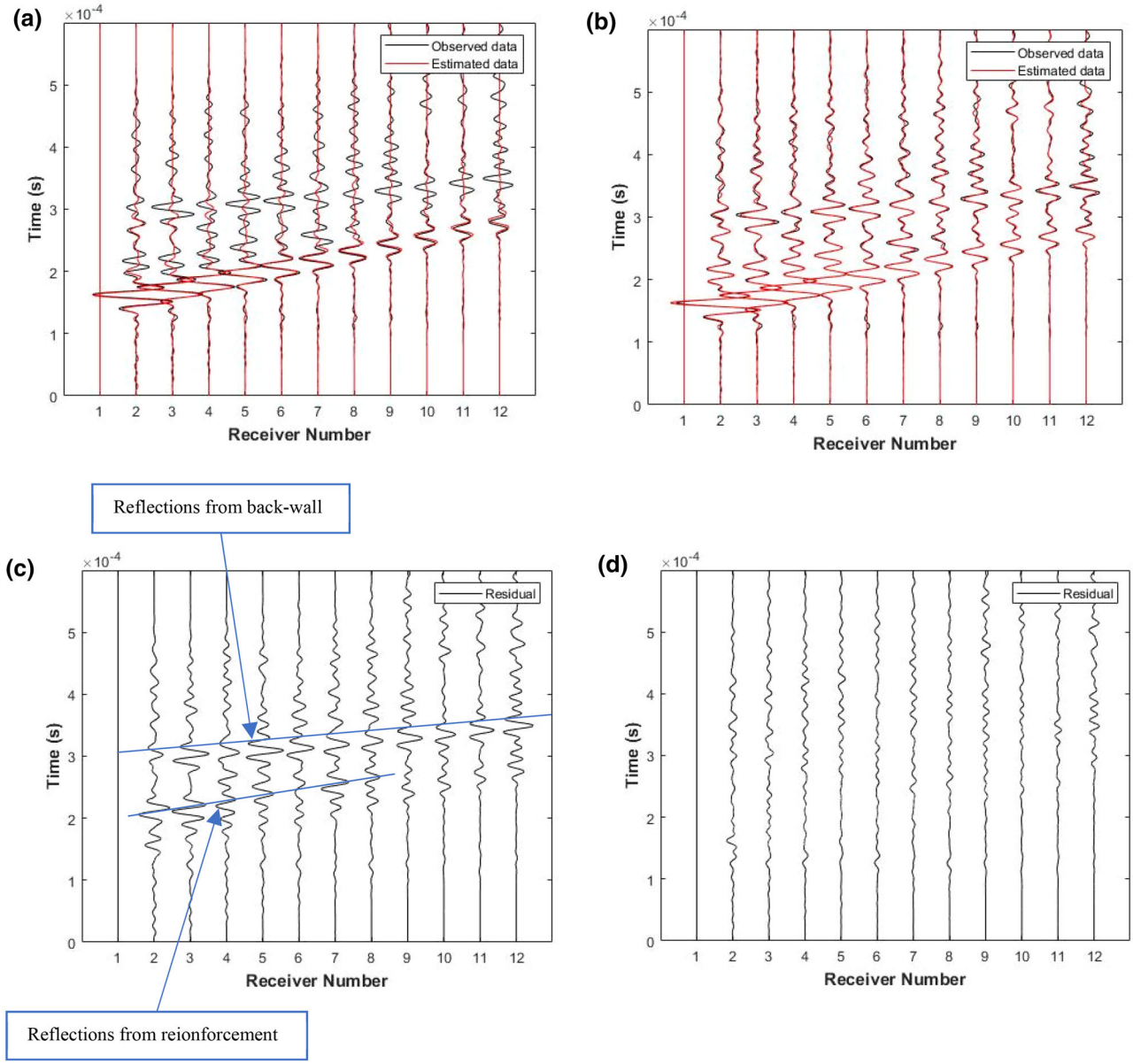

Fig. 6 Waveform comparison for the first shot: **a** observed data and estimated data from the initial model, **b** observed data and estimated data from the final inverted model, **c** initial residual associated with the initial model, and **d** final residual associated with the final inverted model

invert the contrast in the material properties at the concrete-air interface, and cannot accurately invert the air below the slab. Nevertheless, the SH-FWI produced excellent results with accurate rebar locations and back-wall in both density and V_S images.

3.2 Complete Results from Four Concrete Slabs

To build the cross-section of each concrete slab, the ultrasonic waveforms from the five datasets produced from the MIRA were analyzed using the same procedure presented for the sample dataset. The five individual inverted results were combined and processed to reconstruct the cross-section of each slab. Because of the MIRA sampling interval of 200 mm and inverted image of 350 mm length (e.g., Fig. 4d), there is an overlap zone of 150 mm length between two adjacent sampling areas. The density and V_S values within the overlap zone were taken as the average of the corresponding values from the two inverted results. The benefit of the averaging is that some artifacts caused by noise were mitigated, and the images of reinforcement were enhanced.

For the two slabs with rebars of various sizes, the reconstructed cross-sections from the SH-FWI are shown in Figs. 7

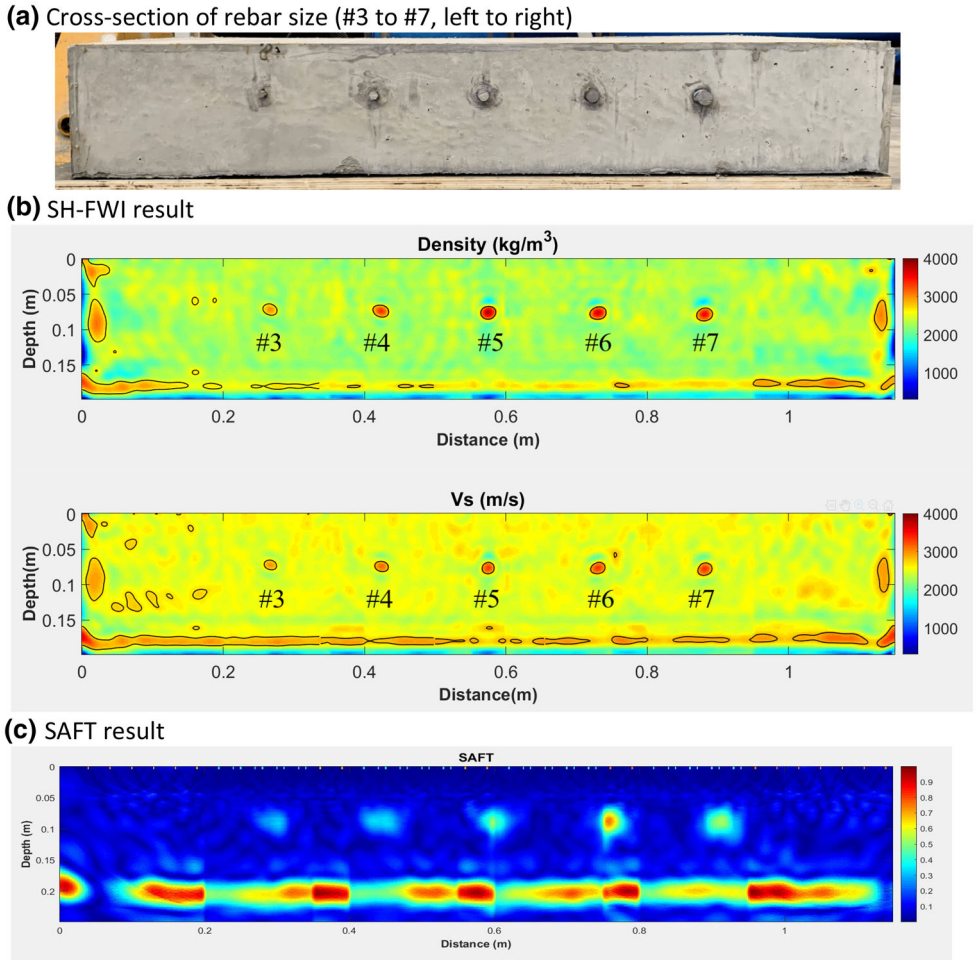

Fig. 7 The inverted cross-section results comparison: **a** true rebars with different sizes of #3, #4, #5, #6, #7 from left to right, respectively, **b** the inverted result from SH-FWI (black circles represent the predicted rebars from the contour map), **c** the SAFT result

and 8, together with the slab photos that show the reinforcement with various sizes from #3 to #14. The cross-sections have a total length of 1150 mm and a depth of 200 mm. Compared to the ground truth (Figs. 7a, 8a), the SH-FWI accurately characterizes the existence and locations of all rebars in both density and V_S images (Figs. 7b, 8b). The double information of density and V_S images provides better reliability of characterized results, which is particularly useful in case of deteriorated structures with low quality data and resulting images [16]. In addition, shear modulus can be computed (density $\times$ $V_S{}^2$) for subsequent engineering analyses such as concrete strength (moduli), stress–strain, and load-deformation behaviors. Lastly, the concrete-air interface is imaged at a distance of 0.19 m from the surface, showing strong agreement with the true thickness of concrete slabs.

To rigorously evaluate rebar sizes, we use contour maps and measure the area of individual inverted rebar within each contour. The goal is to find a common criterion to determine the contour values that can estimate the rebar sizes for all 20 rebars (10 at the same depths and 10 at various depths). As the inverted Vs and density of deeper rebars are lower (less accurate) due to less signal coverage caused by the wave attenuation, common contour values do not work well for deep rebars. However, inverted Vs and density are much higher than those of concrete, we instead used the adaptive contour values based on the difference (contrast) between inverted values of rebars and concrete. Specifically, a contour value of Vs for each rebar is set as:

$$Vs_{contour} = Vs_{concrete} + \gamma[\max(Vs_{rebar}) - Vs_{concrete}], \quad (16)$$

where $Vs_{concrete}$ is the average Vs for concrete (2,500 m/s). Parameter $\max(Vs_{rebar})$ is the maximum inverted Vs of a rebar, which was automatically searched among all inverted Vs values of cells within 5 cm (< half of rebar spacing) around the rebar. The threshold value γ was determined from trial values from 0 to 1.0 at 0.1 interval (10%), and value of 0.4 provided the best prediction for the 10 rebars at the same depth, and thus used in this study. Contour values for density

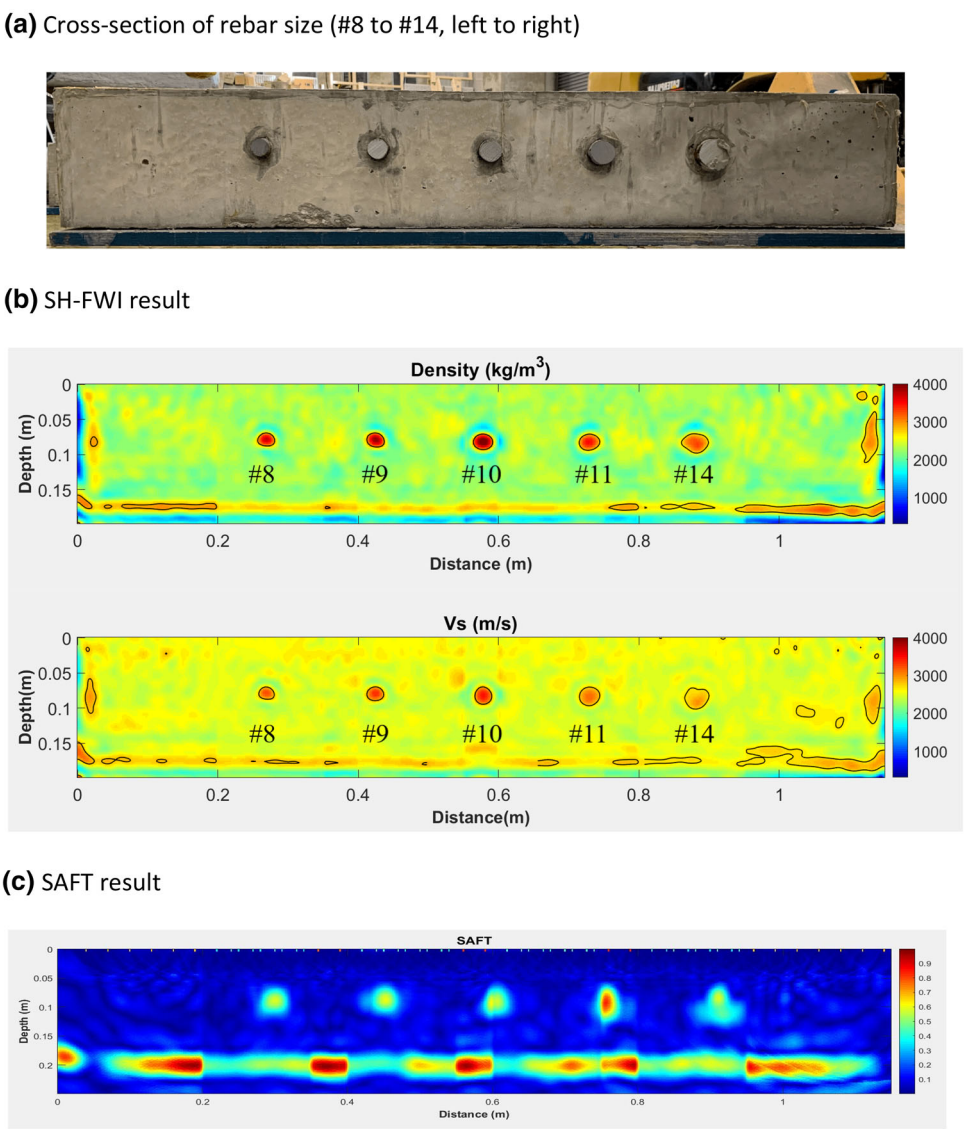

Fig. 8 The inverted cross-section results comparison: **a** true rebars with different sizes of #8, #9, #10, #11, #14 from left to right, respectively, **b** the inverted result from SH-FWI (black circles represent the predicted rebars from the contour map), **c** the SAFT result

were also determined in the same fashion with the same γ of 0.4.

With the contour values from Eq. (16), the contours were automatically generated as shown in Figs. 7b and 8b. The area within each contour of rebars was determined based on the number of cells having values larger than the contour values, and then used to calculate the equivalent diameter of a round rebar. The inverted diameters from SH-FWI and the true diameters are compared in Table 1. Vs profiles produced better estimation of the rebar sizes than the density profiles. Based on inverted Vs, except for the smallest rebar # 3, the difference between the inverted and true sizes is less than 30% for 9 rebars (#4 to #14). Based on the top of contours, the true cover depth of 65 mm is accurately characterized for all rebars.

For comparison, the SAFT [49] was used on the same datasets that used for the SH-FWI analysis. The reconstructed cross-sections from the SAFT are shown in Figs. 7c and 8c. It is noted that the SAFT generates a thicker interface at the back-wall, and a larger depth of 250 mm was used for better visibility. The SAFT successfully identities the locations of all reinforcement however, it cannot distinguish the individual rebar sizes. There is no common contour value that can be used to show all rebars. This is due to the reflection values from SAFT images are quite different at rebar locations (particularly in Fig. 7c). The back-wall is identified at the depth of about 0.20 m. It is worth noting that the SAFT requires much less computational resources and time, and therefore, it remains an efficient technique for real-time structural imaging and inspection. The main limitation of the SH-FWI analysis is the high computing demand (e.g., 20 min for each data set).

For the two slabs with 10 rebars of various depths, the reconstructed results from the SH-FWI and SAFT are shown

Table 1 Comparison of the inverted and true rebar diameters of ten rebars with various sizes (#3 to #14) at the same depth

Rebar number	#3	#4	#5	#6	#7	#8	#9	#10	#11	#14
True diameter (mm)	9.5	12.7	15.9	19.1	22.2	25.4	28.7	32.3	35.8	43.0
Inverted diameter (mm) from density	18.2	19.9	19.8	20.2	20.4	21.4	22.6	24.4	26.0	31.5
Inverted diameter (mm) from Vs	15.8	16.4	16.7	18.2	19.0	19.4	21.8	24.1	27.8	31.8
Error (%) from density	91.5	56.9	24.6	5.7	− 8.0	− 15.7	− 21.4	− 24.4	− 27.3	− 26.7
Error (%) from Vs	66.3	29.4	5.3	− 4.7	− 14.3	− 23.6	− 24.2	− 25.4	− 22.3	− 26.0

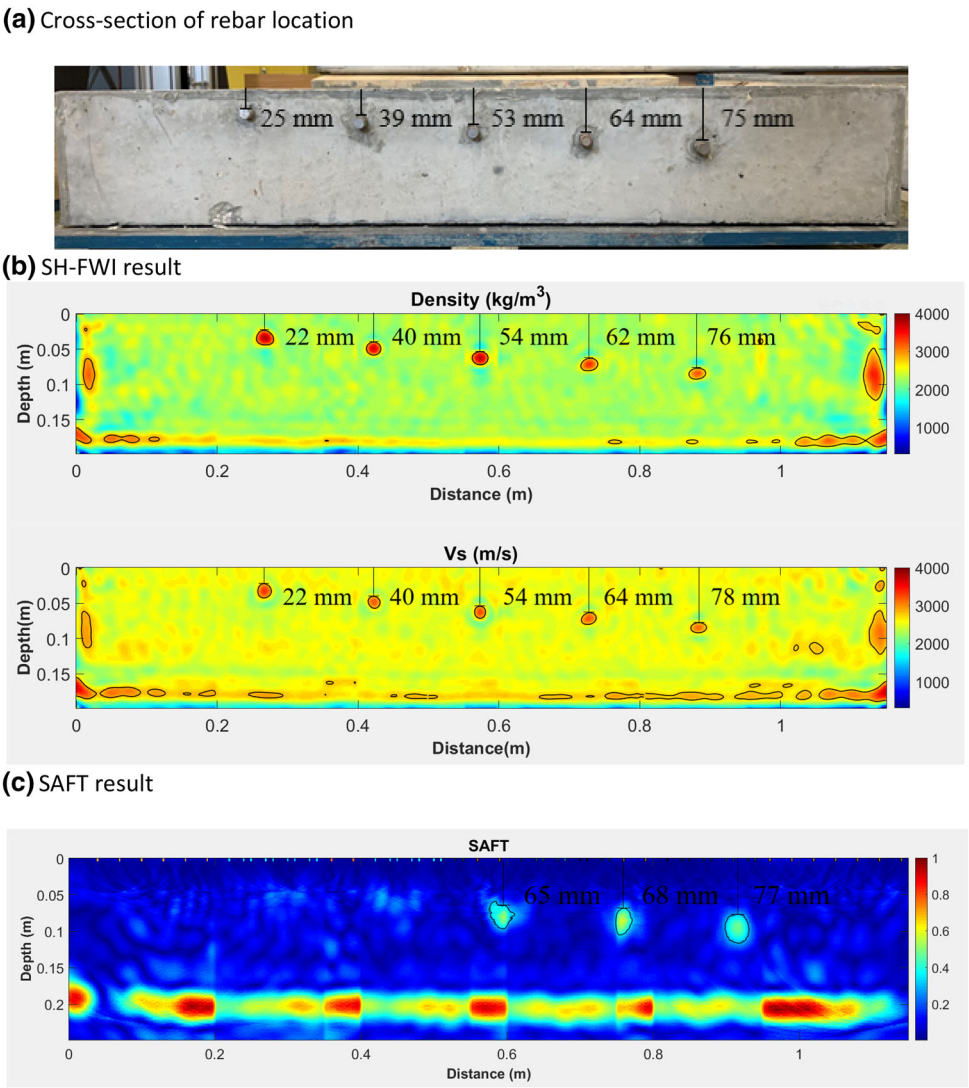

Fig. 9 The inverted cross-section results comparison: **a** true rebars with different embedded depths of 25 mm, 39 mm, 53 mm, 64 mm, 75 mm from left to right, respectively, **b** the inverted result from SH-FWI (length of vertical black line represents the inverted depths), **c** the SAFT result (length of vertical black line represents the inverted depths)

in Figs. 9 and 10, together with the slab photos that show the rebar locations. The true depths of 25 to 140 mm were measured from the free surface to the top edge of the rebars, and shown as the vertical black lines. The inverted SH-FWI results are shown in Figs. 9b and 10b. All 10 rebars are identified, and the thickness of slabs is imaged accurately.

We used the same approach (Eq. 16, with γ of 0.4) to determine contour values and plot contours as shown in Figs. 9b and 10b. The area within each contour of rebars was determined, and then used to calculate the equivalent diameter of a round rebar. Depths of rebar were determined from the free surface to the top of each rebar contour. The inverted rebar sizes and depths are shown in Table 2. Regarding rebar sizes, the inverted sizes from Vs are again more accurate than those from density. Based on Vs images, the difference between the inverted and true sizes is less than less than 33% for all 10

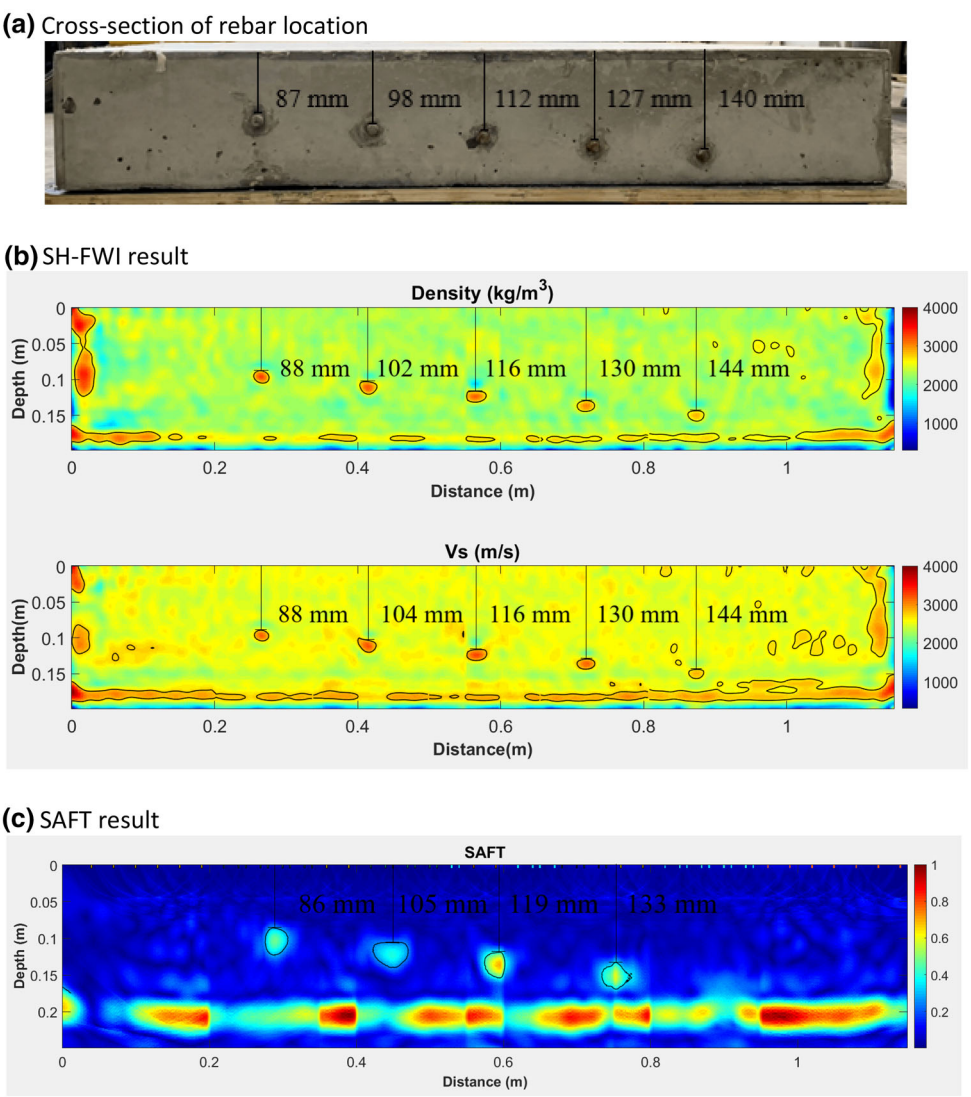

Fig. 10 The inverted cross-section results comparison: **a** true rebars with different embedded depths of 87 mm, 98 mm, 112 mm, 127 mm, 140 mm from left to right, respectively, **b** the inverted result from SH-FWI (length of vertical black line represents the inverted depths), **c** the SAFT result (length of vertical black line represents the inverted depths)

Table 2 Comparison of the inverted and true rebar diameters and depths of ten rebars with the same size (#5) at different depths

True rebar depth (mm)	25	39	53	64	75	87	98	112	127	140
True diameter (mm)	15.9	15.9	15.9	15.9	15.9	15.9	15.9	15.9	15.9	15.9
Inverted diameter (mm) from density	22.8	19.8	20.4	20.8	19.4	19.1	20.7	20.8	19.9	18.5
Inverted diameter (mm) from Vs	19.9	16.7	16.6	18.7	18.2	17.5	20.6	21.0	18.9	16.4
Size error (%) from density	43.3	24.6	28.5	30.8	22.1	20.4	30.1	30.9	25.4	16.2
Size error (%) from Vs	25.4	5.3	4.3	17.9	14.4	10.0	29.3	32.4	18.8	3.3
Inverted depth (mm) from density	22	40	54	62	76	88	102	116	130	144
Inverted depth (mm) from Vs	22	40	54	64	78	88	104	116	130	144
Depth from GPR SAFT (mm)	28	45	59	70	81	94	109	123	136	153
Depth from ultrasonic SAFT (mm)	–	–	65	68	77	86	105	119	133	–
Depth error (%) from density	− 12	2.6	1.9	3.1	1.3	1.1	4.0	3.6	2.3	2.9
Depth error (%) from Vs	− 12	2.6	1.9	0	4	1.1	6.1	3.6	2.3	2.9
Depth error (%) from GPR SAFT	12	15.4	11.3	9.3	8	8	11.2	9.8	7.1	9.3
Depth error (%) from ultrasonic SAFT (mm)	–	–	22.6	6.3	2.7	− 1.1	7.1	6.3	4.7	–

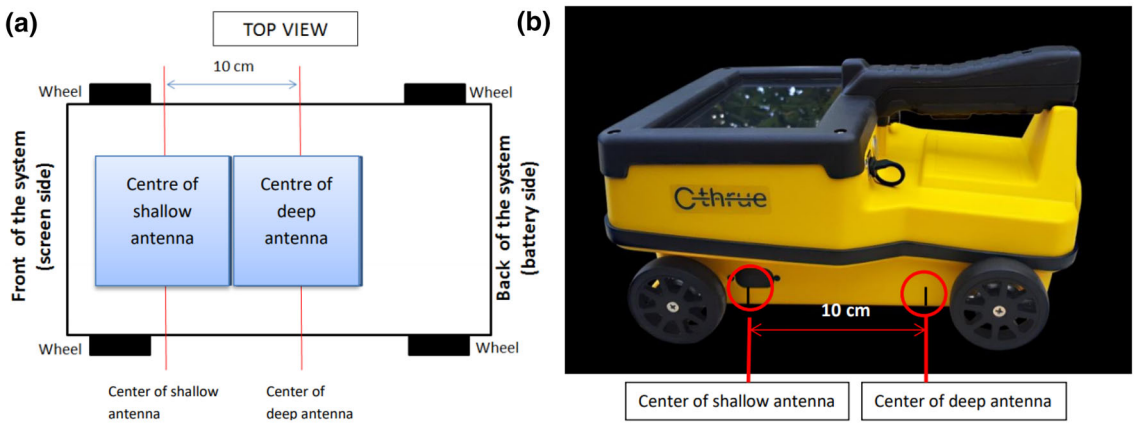

Fig. 11 IDS C-thrue GPR system: **a** top view sketch, and **b** Dual polarization antenna positions

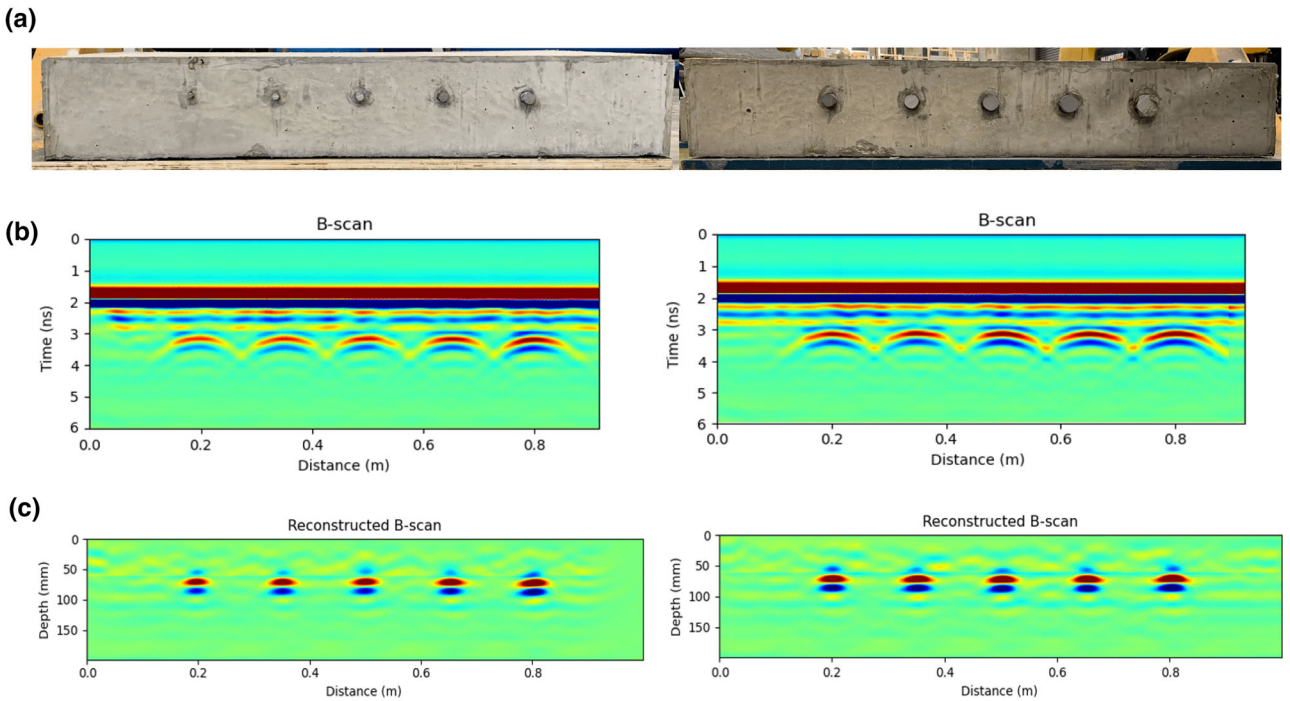

Fig. 12 GPR result of 10 rebar with various sizes (#3 to #14 from left to right) at the same depth: **a** slab photos, **b** raw B-scans, and **c** reconstructed B-scans using the SAFT

rebars. It noted that the threshold value ($\gamma = 0.4$) determined from the 10 rebars at the same depth (trained data) produced good results for 10 other rebars at various depths (predicted data), suggesting it should be used for field data applications. Regarding rebar depths, the inverted depths from both Vs and density well agree with the true depths, with less than 12% difference for all rebars.

The SAFT results are shown in Figs. 9c and 10c, where seven rebars are imaged at embedded depths from 53 to 127 mm. However, the three rebars at shallower and deeper depths are not imaged. The deepest rebar is not identified due to mixing signals reflected from the rebar and back-wall. The two shallow rebars at depths of 25 mm and 39 mm are smeared and muted due to signals reflected from these rebars masked by the dominant surface waves. Using the same concept for plotting contours (Eq. 16 with $\gamma = 0.5$ providing the best depth prediction for ultrasonic SAFT), the predicted cover depths of the seven imaged rebars are included in Figs. 9c and 10c and Table 2 for comparison. Apparently, the SH-FWI results are more accurate. In summary, based on the comparison of the SH-FWI and SAFT results on the four slabs, the presented SH-FWI method better characterizes locations of rebars and distinguishes the sizes of rebars.

3.3 Comparison to GPR Testing

To further assess the SH-FWI advancement, we conducted the ground penetrating radar (GPR) test on the same 4 slabs for comparison. The GPR equipment employed in this study is a 2-GHz GPR system manufactured by IDS GeoRadar. As shown in Fig. 11, it has two antennas oriented perpendicular to each other with a 10-cm spacing distance. The unit has a multi-touch screen for an embedded PC, an integrated control unit (DAD), and four wheels for distance measurement. For data collection on the four slabs (Figs. 12a, 13a), one GPR survey line was conducted for each slab at the center, in the direction perpendicular to the rebars. The antennas' data acquisition parameters were set at 5 A-scans per cm, a time window/range of 12 ns, and digitized to 512 samples per scan. GPR signals were collected without any gain or further filter being applied. The collected data were processed using the GPR SAFT described in [60].

For the two slabs with 10 rebars of various sizes, the raw GPR B-scans and SAFT images are shown in Fig. 12b and c, respectively. The cover depth of 10 rebars can be estimated based on the top of 10 hyperbola (Fig. 12b) or the center of red regions in SAFT images (Fig. 12b). However, it is almost impossible to differentiate individual rebar sizes based on the hyperbolic signatures in raw GPR B-scans or the SAFT images. Compared to the images shown Figs. 7b and 8b, the presented 2D SH-FWI method clearly provides much more information on the rebar sizes.

For the two slabs with 10 rebars at various depths, the raw GPR B-scans and SAFT images are shown in Fig. 13b and c, respectively. Like the first two slabs, the existence and cover depths of rebars can be inferred from the raw B-scans and SAFT images. Specifically, the cover depths measured from GPR SAFT images for those rebars are provided in Table 2. The depth values predicted by the SH-FWI method are more accurate than those measured in GPR SAFT images. Concerning the parameters used for GPR image reconstruction, while the time-zero was located at 0.2 ns before the first positive peak of each A-scan [60], the commonly-used signal velocity of 0.1 m/ns was selected to perform the SAFT algorithm [61]. It should be noted that, the selection of these parameters has a great effect on the cover depths measured in GPR SAFT images.

Finally, the future work will be the application of the 2D SH-FWI method for other concrete defects such as delamination, cracks, honeycombs, concrete segregation, voids, rebar debonding, corrosion, or poorly grouted post-tensioning ducts. As the method characterizes material properties (Vs and density) in mm-cells, these defects are expected to be imaged given that the MIRA signals can penetrate. Besides high frequency data (20–80 kHz) required for high resolution imaging, lower frequency data (10–20 kHz) may be needed for full-volume imaging of large structural components.

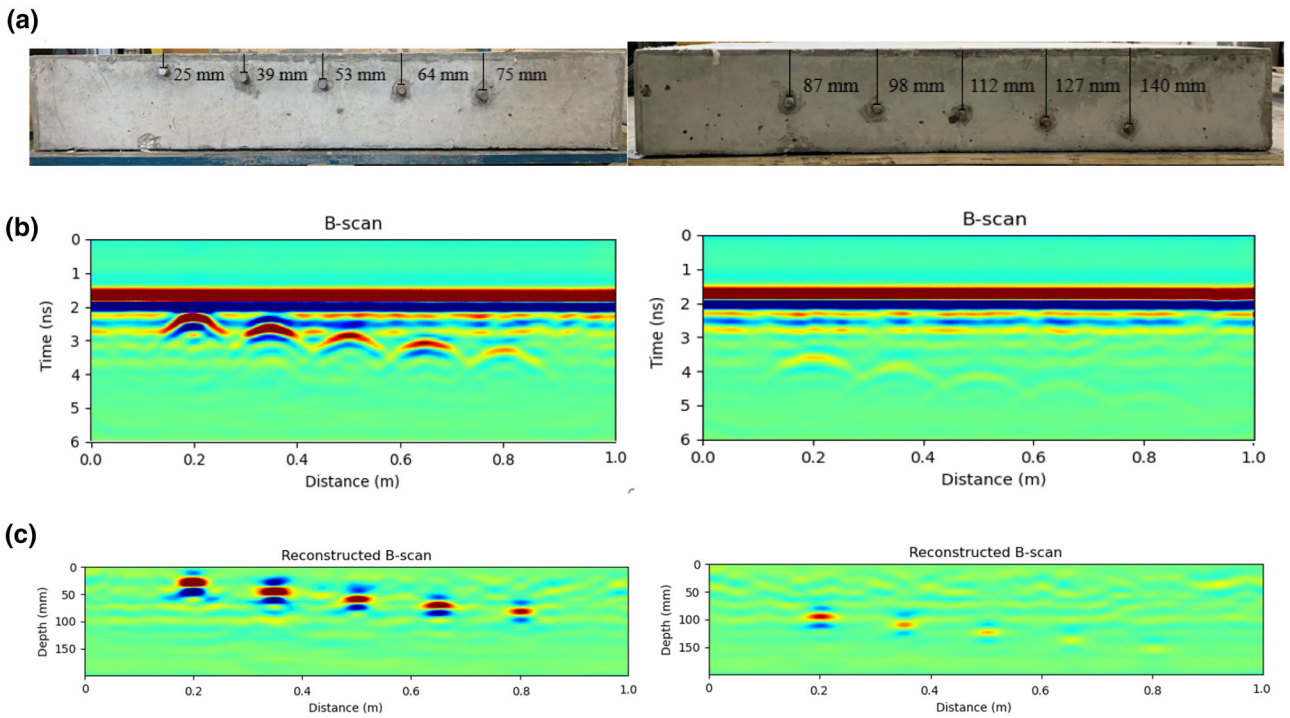

Fig. 13 GPR result of 10 rebar of the same size at various depths: **a** slab photos, **b** raw B-scans, and **c** reconstructed B-scans using the SAFT

4 Conclusions

A first-time application of 2D SH-FWI method on ultrasonic wavefields is presented for determination of rebar locations and sizes in concrete structures. The method was tested on four concrete slabs with 10 rebars of various sizes (#3 to # 14) at the same cover depth of 65 mm, and 10 rebars of the same size (#5) at various depths (25 mm to 140 mm). The ultrasonic SH-wave datasets were recorded using a commercial shear-wave tomography system (MIRA) on the slab surface and analyzed to rebuild the slab cross-sections. Except for the smallest rebars, the method was able to determine the sizes of 95% of rebars (19/20) with less than 33% error, or 80% of rebars (16/20) with less than 26% error. Cover depths of all rebars were characterized with less than 12% error. The ultrasonic SAFT and GPR method were also applied on the same slabs, and they can only identify the depths of rebars, but fail to distinguish the rebar sizes. Based on characterized results, the SH-FWI method is a useful tool for determining rebar locations and sizes in reinforced concrete structures.

References

1. McCann, D.M., Forde, M.C.: Review of NDT methods in the assessment of concrete and masonry structures. NDT E Int. **34**(2), 71–84 (2001). https://doi.org/10.1016/S0963-8695(00)00032-3
2. Dinh, K., Gucunski, N., Duong, T.H.: An algorithm for automatic localization and detection of rebars from GPR data of concrete bridge decks. Autom. Constr. **89**, 292–298 (2018). https://doi.org/10.1016/j.autcon.2018.02.017
3. Algernon, D., Hiltunen, D.R., Ferraro, C.C., Ishee, C.: Rebar detection with cover meter and ultrasonic pulse echo combined with automated scanning system. Transp. Res. Rec. **2251**(1), 123–131 (2011). https://doi.org/10.3141/2251-13
4. Hoegh, K., Khazanovich, L., Yu, H.T.: Ultrasonic tomography for evaluation of concrete pavements. Transp. Res. Rec. **2232**(1), 85–94 (2011). https://doi.org/10.3141/2232-09
5. Hasan, M.I., Yazdani, N.: Ground penetrating radar utilization in exploring inadequate concrete covers in a new bridge deck. Case Stud. Constr. Mater. **1**, 104–114 (2014). https://doi.org/10.1016/j.cscm.2014.04.003
6. Wiwatrojanagul, P., Sahamitmongkol, R., Tangtermsirikul, S., Khamsemanan, N.: A new method to determine locations of rebars and estimate cover thickness of RC structures using GPR data. Constr. Build. Mater. **140**, 257–273 (2017). https://doi.org/10.1016/J.CONBUILDMAT.2017.02.126
7. Utsi, V., Utsi, E.: Measurement of reinforcement bar depths and diameters in concrete. In: Proceedings of the Tenth International Conference on Grounds Penetrating Radar, 2004. GPR 2004, pp. 659–662. IEEE (2004)
8. Zhou, F., Chen, Z., Liu, H., Cui, J., Spencer, B.F., Fang, G.: Simultaneous estimation of rebar diameter and cover thickness by a GPR-EMI dual sensor. Sensors **18**(9), 2969 (2018). https://doi.org/10.3390/s18092969
9. Chang, C.W., Lin, C.H., Lien, H.S.: Measurement radius of reinforcing steel bar in concrete using digital image GPR. Constr. Build. Mater. **23**(2), 1057–1063 (2009). https://doi.org/10.1016/j.conbuildmat.2008.05.018
10. Zhan, R., Xie, H.: GPR measurement of the diameter of steel bars in concrete specimens based on the stationary wavelet transform. Insight-Non-Destruct. Test. Cond. Monit. **51**(3), 151–155 (2009). https://doi.org/10.1784/insi.2009.51.3.151
11. Zanzi, L., Arosio, D.: Sensitivity and accuracy in rebar diameter measurements from dual-polarized GPR data. Constr. Build. Mater. **48**, 1293–1301 (2013). https://doi.org/10.1016/j.conbuildmat.2013.05.009
12. Hasan, M.I., Yazdani, N.: An experimental and numerical study on embedded rebar diameter in concrete using ground penetrating radar. Chin. J. Eng (2016). https://doi.org/10.1155/2016/9714381
13. Mechbal, Z., Khamlichi, A.: Determination of concrete rebars characteristics by enhanced post-processing of GPR scan raw data. NDT E Int. **89**, 30–39 (2017). https://doi.org/10.1016/j.ndteint.2017.03.005
14. Hong, S., Lai, W.W.L., Wilsch, G., Helmerich, R., Helmerich, R., Günther, T., Wiggenhauser, H.: Periodic mapping of reinforcement corrosion in intrusive chloride contaminated concrete with GPR. Constr. Build. Mater. **66**, 671–684 (2014). https://doi.org/10.1016/j.conbuildmat.2014.06.019
15. Dinh, K., Zayed, T., Moufti, S., Shami, A., Jabri, A., Abouhamad, M., Dawood, T.: Clustering-based threshold model for condition assessment of concrete bridge decks with ground-penetrating radar. Transp. Res. Rec. **2522**(1), 81–89 (2015). https://doi.org/10.3141/2522-08
16. Popovics, J.S., Roesler, J.R., Bittner, J., Amirkhanian, A.N., Brand, A.S., Gupta, P., Flowers, K.: Ultrasonic imaging for concrete infrastructure condition assessment and quality assurance. Illinois Center for Transportation (2017)
17. Wang, X., Rister, B., Dadi, G.B.: Evaluating performance of ground penetrating radar (GPR) and pachometers for bridge deck reinforcing steel cover height verification. Construction Research Congress (2020)
18. Virieux, J., Operto, S.: An overview of full-waveform inversion in exploration geophysics. Geophysics **74**(6), WCC1–WCC26 (2009). https://doi.org/10.1190/1.3238367
19. Pratt, R.G.: Seismic waveform inversion in the frequency domain; Part 1, Theory and verification in a physical scale model. Geophysics **64**(3), 888–901 (1999). https://doi.org/10.1190/1.1444597
20. Shipp, R.M., Singh, S.C.: Two-dimensional full wavefield inversion of wide-aperture marine seismic streamer data. Geophys. J. Int. **151**(2), 325–344 (2002). https://doi.org/10.1046/j.1365-246X.2002.01645.x
21. Ravaut, C., Operto, S., Improta, L., Virieux, J., Herrero, A., Dell'Aversana, P.: Multiscale imaging of complex structures from multifold wide-aperture seismic data by frequency-domain full-waveform tomography: application to a thrust belt. Geophys. J. Int. **159**(3), 1032–1056 (2004). https://doi.org/10.1111/j.1365-246X.2004.02442.x
22. Sheen, D.H., Tuncay, K., Baag, C.E., Ortoleva, P.J.: Time domain Gauss—Newton seismic waveform inversion in elastic media. Geophys. J. Int. **167**(3), 1373–1384 (2006). https://doi.org/10.1111/j.1365-246X.2006.03162.x
23. Sears, T.J., Singh, S.C., Barton, P.J.: Elastic full waveform inversion of multi-component OBC seismic data. Geophys. Prospect. **56**(6), 843–862 (2008). https://doi.org/10.1111/j.1365-2478.2008.00692.x
24. Prieux, V., Brossier, R., Operto, S., Virieux, J.: Multiparameter full waveform inversion of multicomponent ocean-bottom-cable data from the Valhall field. Part 1: imaging compressional wave speed, density and attenuation. Geophys. J. Int. **194**(3), 1640–1664 (2013). https://doi.org/10.1093/gji/ggt177
25. Métivier, L., Bretaudeau, F., Brossier, R., Operto, S., Virieux, J.: Full waveform inversion and the truncated Newton method: quantitative imaging of complex subsurface structures. Geophys.

Prospect. **62**(6), 1353–1375 (2014). https://doi.org/10.1111/1365-2478.12136
26. Tran, K.T., McVay, M., Faraone, M., Horhota, D.: Sinkhole detection using 2D full seismic waveform tomographySinkhole detection by FWI. Geophysics **78**(5), R175–R183 (2013). https://doi.org/10.1190/geo2013-0063.1
27. Tran, K.T., Sperry, J.: Application of 2D full-waveform tomography on land-streamer data for assessment of roadway subsidence. Geophysics **83**(3), EN1–EN11 (2018). https://doi.org/10.1190/geo2016-0550.1
28. Epanomeritakis, I., Akçelik, V., Ghattas, O., Bielak, J.: A Newton-CG method for large-scale three-dimensional elastic full-waveform seismic inversion. Inverse Prob. **24**(3), 034015 (2008). https://doi.org/10.1088/0266-5611/24/3/034015
29. Fichtner, A., Kennett, B.L., Igel, H., Bunge, H.P.: Full seismic waveform tomography for upper-mantle structure in the Australasian region using adjoint methods. Geophys. J. Int. **179**(3), 1703–1725 (2009). https://doi.org/10.1111/j.1365-246X.2009.04368.x
30. Tape, C., Liu, Q., Maggi, A., Tromp, J.: Seismic tomography of the southern California crust based on spectral-element and adjoint methods. Geophys. J. Int. **180**(1), 433–462 (2010). https://doi.org/10.1111/j.1365-246X.2009.04429.x
31. Vigh, D., Kapoor, J., Moldoveanu, N., Li, H.: Breakthrough acquisition and technologies for subsalt imaging. Geophysics **76**(5), WB41–WB51 (2011). https://doi.org/10.1190/geo2010-0399.1
32. Warner, M., Ratcliffe, A., Nangoo, T., Morgan, J., Umpleby, A., Shah, N., Conroy, G.: Anisotropic 3D full-waveform inversion. Geophysics **78**(2), R59–R80 (2013). https://doi.org/10.1190/geo2012-0338.1
33. Ha, W., Kang, S.G., Shin, C.: 3D Laplace-domain waveform inversion using a low-frequency time-domain modeling algorithm. Geophysics **80**(1), R1–R13 (2015). https://doi.org/10.1190/geo2013-0332.1
34. Métivier, L., Brossier, R., Mérigot, Q., Oudet, E., Virieux, J.: An optimal transport approach for seismic tomography: application to 3D full waveform inversion. Inverse Prob. **32**(11), 115008 (2016). https://doi.org/10.1088/0266-5611/32/11/115008
35. Trinh, P.T., Brossier, R., Métivier, L., Tavard, L., Virieux, J.: Efficient time-domain 3D elastic and viscoelastic full-waveform inversion using a spectral-element method on flexible Cartesian-based mesh. Geophysics **84**(1), R61–R83 (2019). https://doi.org/10.1190/geo2018-0059.1
36. Nguyen, T.D., Tran, K.T.: Site characterization with 3D elastic full-waveform tomography Geotechnical site characterization with 3D FWI. Geophysics **83**(5), R389–R400 (2018). https://doi.org/10.1190/geo2017-0571.1
37. Mirzanejad, M., Tran, K.T.: 3D viscoelastic full waveform inversion of seismic waves for geotechnical site investigation. Soil Dyn. Earthq. Eng. **122**, 67–78 (2019). https://doi.org/10.1016/j.soildyn.2019.04.005
38. Tran, K.T., Mirzanejad, M., McVay, M., Horhota, D.: 3-D time-domain Gauss-Newton full waveform inversion for near-surface site characterization. Geophys. J. Int. **217**(1), 206–218 (2019). https://doi.org/10.1093/gji/ggz020
39. Tran, K.T., Nguyen, T.D., Hiltunen, D.R., Stokoe, K., Menq, F.: 3D full-waveform inversion in time-frequency domain: field data application. J. Appl. Geophys. (2020). https://doi.org/10.1016/j.jappgeo.2020.104078
40. Mirzanejad, M., Tran, K.T., McVay, M., Horhota, D., Wasman, S.J.: Coupling of SPT and 3D full waveform inversion for deep site characterization. Soil Dyn. Earthq. Eng. **136**, 106196 (2020). https://doi.org/10.1016/j.soildyn.2020.106196
41. Mirzanejad, M., Tran, K.T., McVay, M., Horhota, D., Wasman, S.J.: Sinkhole detection with 3D full seismic waveform tomography. Geophysics **85**(5), B169–B179 (2020). https://doi.org/10.1190/geo2019-0490.1
42. Rao, J., Ratassepp, M., Fan, Z.: Limited-view ultrasonic guided wave tomography using an adaptive regularization method. J. Appl. Phys. **120**(19), 194902 (2016). https://doi.org/10.1063/1.4967790
43. Rao, J., Ratassepp, M., Fan, Z.: Investigation of the reconstruction accuracy of guided wave tomography using full waveform inversion. J. Sound Vib. **400**, 317–328 (2017). https://doi.org/10.1016/j.jsv.2017.04.017
44. Nguyen, L.T., Modrak, R.T.: Ultrasonic wavefield inversion and migration in complex heterogeneous structures: 2D numerical imaging and nondestructive testing experiments. Ultrasonics **82**, 357–370 (2018). https://doi.org/10.1016/j.ultras.2017.09.011
45. Jalinoos, F., Tran, K.T., Nguyen, T.D., Agrawal, A.K.: Evaluation of bridge abutments and bounded wall type structures with ultraseismic waveform tomography. J. Bridg. Eng. **22**(12), 04017104 (2017). https://doi.org/10.1061/(ASCE)BE.1943-5592.0001150
46. Tran, K.T., Jalinoos, F., Nguyen, T.D., Agrawal, A.K.: Evaluation of bridge abutment with ultraseismic waveform tomography: field data application. J. Nondestr. Eval. **38**(4), 95 (2019). https://doi.org/10.1007/s10921-019-0631-4
47. Nguyen, T.D., Tran, K.T., Gucunski, N.: Detection of bridge-deck delamination using full ultrasonic waveform tomography. J. Infrastruct. Syst. **23**(2), 04016027 (2017). https://doi.org/10.1061/(ASCE)IS.1943-555X.0000323
48. Chen, R., Tran, K.T., Wang, Y.: Time-domain full waveform inversion of SH-and Love-waves for geotechnical site characterization. Near Surf. Geophys. (2021). https://doi.org/10.1002/nsg.12137
49. Schickert, M., Krause, M., Müller, W.: Ultrasonic imaging of concrete elements using reconstruction by synthetic aperture focusing technique. J. Mater. Civ. Eng. **15**(3), 235–246 (2003). https://doi.org/10.1061/(ASCE)0899-1561(2003)15:3(235)
50. Virieux, J.: SH-wave propagation in heterogeneous media: velocity-stress finite-difference method. Geophysics **49**(11), 1933–1942 (1984). https://doi.org/10.1190/1.1441605
51. Levander, A.R.: Fourth-order finite-difference P-SV seismograms. Geophysics **53**(11), 1425–1436 (1988). https://doi.org/10.1190/1.1442422
52. Komatitsch, D., Martin, R.: An unsplit convolutional perfectly matched layer improved at grazing incidence for the seismic wave equation. Geophysics **72**(5), SM155–SM167 (2007). https://doi.org/10.1190/1.2757586
53. Plessix, R.E.: A review of the adjoint-state method for computing the gradient of a functional with geophysical applications. Geophys. J. Int. **167**(2), 495–503 (2006). https://doi.org/10.1111/j.1365-246X.2006.02978.x
54. Tikhonov, A.N., Arsenin, V.Y.: Solutions of Ill-Posed Problems, pp. 1–30. Springer, New York (1977)
55. Nocedal, J., Wright, S.: Numerical Optimization. Springer, New York (2006)
56. Zhang, Z., Huang, L., Lin, Y.: Double-difference elastic-waveform inversion with weighted gradients for monitoring EGS reservoirs. In: Thirty-Seventh Workshop on Geothermal Reservoir Engineering. Stanford University, California (2012)
57. Busch, S., van der Kruk, J., Bikowski, J., Vereecken, H.: Quantitative conductivity and permittivity estimation using full-waveform inversion of on-ground GPR data. Geophysics **77**(6), H79–H91 (2012). https://doi.org/10.1190/geo2012-0045.1
58. Ernst, J.R., Green, A.G., Maurer, H., Holliger, K.: Application of a new 2D time-domain full-waveform inversion scheme to crosshole radar data. Geophysics **72**(5), J53–J64 (2007). https://doi.org/10.1190/1.2761848

59. Schäfer, M., Groos, L., Forbriger, T., Bohlen, T.: On the effects of geometrical spreading corrections for a 2D full waveform inversion of recorded shallow seismic surface waves. In: 74th EAGE Conference and Exhibition incorporating EUROPEC 2012. European Association of Geoscientists & Engineers, pp. cp-293–00298. https://doi.org/10.3997/2214-4609.20148327 (2012)
60. Dinh, K., Gucunski, N., Tran, K.T., Novo, A., Nguyen, T.: Full-resolution 3D imaging for concrete structures with dual-polarization GPR. Autom. Constr. **125**, 103652 (2021). https://doi.org/10.1016/j.autcon.2021.103652
61. Dinh, K., Gucunski, N., Zayed, T.: Automated visualization of concrete bridge deck condition from GPR data. NDT E Int. **102**, 120–128 (2019). https://doi.org/10.1016/j.ndteint.2018.11.015